AI-powered pan-species computational pathology: bridging clinic and wildlife care

Khalid AbdulJabbar[1,2+], Simon P. Castillo[1,2+], Katherine Hughes[3], Hannah Davidson[4,5], Amy M. Boddy[6], Lisa M. Abegglen[7,8], Elizabeth P. Murchison[3,9], Trevor A. Graham[1,5], Simon Spiro[4], Chiara Palmieri[10], Yinyin Yuan[1,2*]

Affiliations:

[1]Centre for Evolution and Cancer, The Institute of Cancer Research, London, UK
[2]Division of Molecular Pathology, The Institute of Cancer Research, London, UK
[3]Department of Veterinary Medicine, University of Cambridge, Madingley Road, Cambridge, UK.
[4]Zoological Society of London, London, UK.
[5]Centre for Genomics and Computational Biology, Barts Cancer Institute, Queen Mary University of London, Charterhouse Sq, London, UK.
[6]Department of Anthropology, University of California Santa Barbara, Santa Barbara, CA, USA.
[7]Department of Pediatrics and Huntsman Cancer Institute, University of Utah, Salt Lake City, UT, USA.
[8]PEEL Therapeutics, Inc., Salt Lake City, UT, USA and Haifa, Israel.
[9]Transmissible Cancer Group, Department of Veterinary Medicine, University of Cambridge, Cambridge, UK.
[10]School of Veterinary Science, The University of Queensland, 4343 Gatton, Queensland, Australia.
[+]Authors contributed equally. *Correspondence to Yinyin Yuan (yinyin.yuan@icr.ac.uk)

Abstract:

Cancers occur across species. Understanding what is consistent and varies across species can provide new insights into cancer initiation and evolution, with significant implications for animal welfare and wildlife conservation. We built the pan-species cancer digital pathology atlas (PANCAD) and conducted the first pan-species study of computational comparative pathology using a supervised convolutional neural network algorithm trained on human samples. The artificial intelligence algorithm achieves high accuracy in measuring immune response through single-cell classification for two transmissible cancers (canine transmissible venereal tumour, 0.94; Tasmanian devil facial tumour disease, 0.88). Furthermore, in 18 other vertebrate species (mammalia=11, reptilia=4, aves=2, and amphibia=1), accuracy (0.57-0.94) was influenced by cell morphological similarity preserved across different taxonomic groups, tumour sites, and variations in the immune compartment. A new metric, named morphospace overlap, was developed to guide veterinary pathologists towards rational deployment of this technology on new samples. This study provides the foundation and guidelines for transferring artificial intelligence technologies to veterinary pathology based on a new understanding of morphological conservation, which could vastly accelerate new developments in veterinary medicine and comparative oncology.

Introduction

Cancers occur with phenotypically similar forms across the tree of life[1–4]. Understanding the conserved and diverged aspects of cancer across species can help answer questions about the origin and fundamental processes of its evolution. Immediate and practical advances from pan-species studies provide new tools and valuable insights into tumorigenesis and cancer resistance[5–8], leading to improved cancer care for humans and non-human animals. Specifically, transmissible cancers presented in dogs and Tasmanian devils[9,10] are among the few known naturally occurring clonally transmissible cancers[11]. How transmissible cancers escape immune surveillance remains unclear and is of central importance to understanding their biology and cell to cell interactions.

Despite significant resources in companion animal care, clinical treatments options are limited for a few aggressive cancers in dogs[12,13] that represent one of the best models of human cancer[14]. Beyond domesticated species, various studies have identified valuable models in wildlife[15]. For instance, the naturally-emerging urogenital carcinoma in California sea lions[16] and papillomavirus triggering brain tumours in raccoons[15] are remarkable examples of pathogen-driven neoplasms. Animals managed in zoological institutes also exhibit occurrence of neoplastic growth according to several international studies, including, a 10-year survey in the Taipei zoo, Taiwan[17], a study of cancer development in vertebrates in French zoological parks[18], a 42-years of mammals necropsy data compilation from the San Diego Zoo, United States[19], and a report on renal lesions followed by neoplastic and inflammatory responses in captive wild felids in Germany[20]. Studies of these animals can provide unique insights into the biology and evolution of cancer across the tree of life towards improving animal welfare by early detection and helping conserve endangered species[21,22].

Challenges for establishing a unified comparative oncology agenda include sample collection, data management, analysis, and integration[23–27]. These can be tackled by incorporating artificial intelligence (AI) algorithms, which can empower veterinary pathology and help dissect the complexity of cancer across species and scales, from genes to epidemiology. Computational pathology powered by AI has revolutionised the study of human cancers and helped improve our understanding of the immune microenvironment[28]. In contrast to human cancer management, we lack systematic and standardised AI protocols and digital archiving and analysis of samples to study animal cancers; hence, veterinary research has not fully adopted digital pathology[25] although efforts are being made to move forward internationally adopted guidelines for tumour pathology[27].

Hence, we propose AI has the power to fuel pan-species tumour histology and efficiently manage data-related bottlenecks. Thus far, computational pathology in the study of non-human cancers, and non-human pathology in general, is very limited[24,25]. Convolutional neural networks have been applied to detect mitotic activity from histological slides of canine cancers[13,29]. In sheep, deep learning has been employed to delineate growth phases of mammary development[30]. Other machine learning techniques have been used to classify a common gastrointestinal disease in cats[31]. Along with computational pathology, incorporating AI into the veterinary practice of imaging techniques such as CT scans, magnetic resonance imaging, and

positron emission tomography[32] encourages the development of integrative clinical care. Such an integrative approach promises to direct precision medicine in veterinary oncology by tailoring strategies for individual patients. It includes classifying patients who differ in their treatment response and/or prognostic outcomes.

In this work, we explore and exploit the conservatism of cell morphology in neoplasias across species by applying an AI tool trained in human lung cancer[33] (Fig 1). We evaluate the accuracy of this AI tool in mapping tumour cells distribution and lymphocytic infiltration in histological tissues from transmissible cancers and its generalisability to 18 other species. To the best of our knowledge, this is the first effort to apply computational pathology algorithms to transmissible cancers and pan-species pathology beyond mammals, thereby decoding the composition of cells in tumours across species. Our approach aims to pave the way for pan-species comparative pathology and contribute to understanding the emergence and prevalence of cancer in nature.

Results

Collection and quality control for veterinary histology samples

Ten hematoxylin and eosin (H&E)-stained tumour samples from 3 individuals with Tasmanian devil facial tumour disease 1 and 2 (DFT1 and DFT2) and 6 with canine transmissible venereal tumour (CTVT) were collected and digitalised from the Transmissible Cancers Group, University of Cambridge. Of these, 7 passed visual quality control for image analysis. One representative slide was chosen by the pathologists for each species considering scanning resolution and level of immune infiltration in the tumour microenvironment. In addition, H&E samples from 18 species were selected from the Zoological Society of London's (ZSL) pathological archive and digitalised (classes Mammalia = 11 species, Reptilia = 4, Aves = 2, and Amphibia = 1). The neoplastic lesions were broadly categorised into five main tumour groups: round-cell (n = 4), epithelial (n = 9), mesenchymal (n = 4), neuroendocrine (n=2) and sex-cord stromal (n=1) tumours. A rich, pan-species digital pathology atlas was created, providing digital slide images, digitalisation and quality control protocols, and pathological annotations described below.

Transferring AI technologies to non-human species

A deep learning pipeline tailored for human lung cancer (predominantly lung adenocarcinoma, including lung squamous cell carcinoma[33], Fig. 1A) was applied without modification to all 20 H&E samples. Briefly, this pipeline identifies the precise location of individual cells in each H&E and classifies them based on nuclear morphology in one of four cell types: tumour cells, lymphocytes, stromal cells (fibroblasts and endothelial cells) and 'other' cells (macrophages, pneumocytes and non-identifiable cells) (Fig. 1B-C). We evaluated the accuracy of the convolutional neural network (CNN) with 14,570 cancer, lymphocyte, and stromal single-cell annotations from two board-certified specialist veterinary pathologists (CP and KH). For each

slide, we computed the algorithm's balanced single-cell classification accuracy (BCAcc, Table 1), as well as F1 score, precision, sensitivity and specificity (Figs S1-S2).

For evaluating the accuracy in classifying cells by the algorithm, we compared its predictions against veterinary pathologists' annotations. The algorithm's average balanced accuracy across cell classes showed a diverse range of variation between and within tumour groups (Figs. 2A, S1-S2). Tumour types have the same overall accuracy for cell classification based on the balanced classification accuracy values (LR test, overall BCAcc averaged across samples = 0.81; LR test, $\chi^2[3] = 0.314$, $p = 0.957$). Moreover, despite the heterogeneous number of annotations per tumour type (Fig. 2B), the balanced accuracy was not associated with the number of annotations (Spearman's $\rho = 0.088$, $p = 0.71$) (Fig. 2B-C).

Consistent accuracy across tumour types but higher in mammals

Overall, the model's best performance was mainly in mammals (Fig. 3). In particular, the AI algorithm achieves high accuracy in measuring immune response for the two transmissible cancers (canine transmissible venereal tumour - CTVT, 0.94; Tasmanian devil facial tumour disease- DFTD, 0.88). The canine transmissible venereal tumour (in *Canis l. familiaris*) exhibited the best accuracy across all 20 species (overall precision = 0.98, F1 and BCAcc = 0.94, Fig. 3). Surprisingly, in the metastatic sarcoma in a snake (*Gonyosoma oxycephalum*), the CNN also reached a high accuracy (Fig. 4A, overall precision = 0.89, F1 = 0.89 and BCAcc = 0.91).

In the 18 other vertebrate species (mammalia=11, reptilia=4, aves=2, and amphibia=1), accuracy varies (0.57-0.94). The performance of cancer cells and lymphocyte classification, measured as balanced accuracy, did not vary between tumour types (LR test, cancer cells: median = 0.825, $\chi^2[3] = 1.358$, $p = 0.715$; lymphocytes: median = 0.915, $\chi^2[3] = 0.308$, $p = 0.959$). However, the classification accuracy of stromal cells differs between tumour types (LR test, median = 0.773,$\chi^2[3] = 10.308$, $p = 0.016$), with p-adjusted significant only for differences between epithelial-round cell (z-test, estimate = -0.092, SE = 0.031, z = -3.073, p = 0.018) and mesenchymal-round cell tumour types (estimate = -0.121, SE = 0.039, z = -3.073, p = 0.011). All other comparisons have a p-value higher than 0.05. Surprisingly, in both cases where we reported significant differences, the balanced accuracy of stromal cells in round-cell tumour types was higher than mesenchymal or epithelial tumour types. In our cohort, the round-cell tumour types were present in the dog (*Canis familiaris*), the Tasmanian devil (*Sarcophillus harrisii*), the pygmy goat (*Capra hircus*) and the ring-tailed coati (*Nasua nasua*). These results show a high classification accuracy of the model consistent with expert pathologists' annotations across tumour types for cancer cells and lymphocytes and slight variations in the case of stromal cells.

Species and cancer-specific challenges

The detection of cancer cells presented more challenging classifications in lymphosarcoma from the common goat (*Capra hircus*), the ring-tailed coati (*Nasua nasua*) and in lipoma from the

dwarf crocodile (*Osteolaemus tetraspis*), which by their cell morphology and tissue architecture may be difficult to be classified by an algorithm trained with epithelial cells from human lung adenocarcinoma (Fig. 4B). These results suggest that the accuracy of computational pathology at single-cell resolution depends on the type of target cancer and its degree of differentiation from the training cancer type. Morphologically complex cancers that drastically change their morphological features or cancers with a high degree of similarity to the normal cells (e.g. lymphosarcoma) represent significant hurdles for transfer learning.

Morphological preservation across species

To explore the morphological similarity between human and non-human samples, which could explain the accuracy of the AI algorithm, we visualised the morphological space of ~32K cells annotated by expert pathologists using principal component analysis (Fig 5). The PCA analysis was used for dimension reduction (Fig 5) of the 27 features extracted by the AI algorithm at the individual cell level (Table S2). The first three PCA dimensions account for 84.1% of the morphological variance (Fig S3A). The first dimension explains 49.4% of the morphological variance, and the cell features with the highest contributions to that explained variance are associated with nucleus size (area, perimeter, diameter, radius, convex area) and maximum intensity in the colour channels (Fig S3B). These variables are positively correlated with the first dimension, with high importance to explaining individual cells' position in the morphological space (Fig S3C). The overlap of the volumes in PCA space suggests a high degree of morphological similarity between human and non-human cells (Table S3). For non-human lymphocytes, 84.55% of their morphological space intersects with the human lymphocyte morphospace. And for non-human tumour cells volume, which shows higher morphological variability, 86.49% of its volume is captured by human tumour cells' volume.

Morphospace overlap as a new guidance metric

To further dissect the relationship between the AI performance and morphological similarity across species, we developed a new metric, termed morphospace overlap, as the average of overlaps of cancer cell/lymphocyte morphological space between a species and humans. We found that the AI model's balanced accuracy is positively correlated with morphospace overlap (Pearson's correlation = 0.68, p=0.001; Fig 5B), suggesting that the AI model performed better on species sharing higher morphological similarity with human cells. Species-specific analyses revealed further understanding of the model's performance. Among the tissues with higher balanced accuracy and high morphospace overlap are dog's CTVT (Fig 5C), Tasmanian devils' DFTD (Fig 5D) and snake's sarcoma (Fig 5E) (morphospace overlap (%) = 82.6, 72.2, and 83.4, balanced accuracy = 0.94, 0.88, and 0.91, respectively) and the goat's lymphosarcoma (Fig 5F) as one of the challenging cases, with smaller morphological overlap between its tumour cells and human's cells (morphospace overlap (%) = 47.4, balanced accuracy = 0.7). Species with >70% morphospace overlap had an average of 87.5% balanced accuracy (range 79-94%), and species with >80% morphospace overlap averaged 88% balanced accuracy (range 80-94%). Thus, this new metric may be a useful tool for pathologists to determine the usability of our AI tool.

Discussion

Comparative oncology pursues the understanding of cancer as a shared phenomenon among species. Here, we have explored the potential of AI through automated pathological image analysis to study cancer morphology and immune response across the tree of life. Previous studies have often been limited to a single species, with applications mainly focused on canine and mouse models (e.g.,[8,13,34]). To the best of our knowledge, this is the first study of computational pathology that includes tumours from vertebrates beyond mammals, such as aves, reptiles and one amphibian. Although the algorithm was trained on human samples, it could distinguish three major cell types with remarkable accuracy in most of the species (19/20 species reached an accuracy ≥ 70% and 12/20 species ≥ 80%). Broadly, our comparative analysis revealed that regardless of species, morphological conservation across species dictates that cells can be detected and correctly classified by a human specimen-trained AI, fostering our endeavour to develop pan-species computational pathology.

Since the model was trained with human epithelial tumour samples, the specimens for testing include other tumour types such as mesenchymal, round cell and neuroendocrine that can have a greater variety of cell morphology, and such diversity of species, and tumour types and sites, likely underpins the wide range of accuracy (0.57-0.94) achieved. For example, in the case of the malignant spindle cell tumour (haemangiosarcoma in a lemur), the neoplastic endothelial cells have large, rounded nuclei, which may appear morphologically similar to that of epithelial cancer cells, as opposed to the elongated nuclei of normal endothelial cells (Fig. 4C). Similarly, for the chimpanzee (*Pan troglodytes*) with a spindle cell sarcoma, the neoplastic fibroblasts are hard to differentiate from reactive fibroblasts with a spindle shape (Fig. 4D). This is a challenge both for the automated analysis and manually by pathologists. Another challenging aspect is the immune compartment, which is highly variable among mammals, birds and reptiles[35], imposing difficulties that seem complicated to pass with a generic algorithm. Moreover, this is amplified when evaluating cancer affecting the lymphatic tissue, such as lymphosarcoma in the coati (*N. nasua*) and pygmy goat (*C. hircus*), where the white blood cell morphology is altered. Lymphosarcoma cells generally appear similar to normal lymphoid cells, resulting in narrow discriminability chances. In those cases, it may be appropriate to take alternative strategies such as re-train the model, test available models for lymphosarcoma (e.g., [36]), or develop a new model incorporating other tissue characteristics. To address this issue, we developed a new metric, named morphospace overlap, to guide pathologists who wish to apply the AI tools to their samples based on morphological similarity.

Based on our data, the transferability of existing AI technologies developed for humans to the veterinary domain may be significantly higher than previously thought. Medical treatment for animals has dramatically improved in veterinary clinics, zoological institutions and even wildlife veterinarians[37], leading to better options for diagnosing and treating cancer in animal patients[23]. Despite these significant advances in veterinary oncology[38], there are significant constraints and limited availability of veterinary specialists[39], and consequently, digital tools are not widely used[24,25]. Thus, computational pathology for different species and tumour types will bring

tremendous advances for clinical veterinary care and comparative oncology research[24,40]. Many of the advantages are similar to those for human pathology, with the greatest benefits being accessibility to veterinary pathologists, time saved and increased diagnostic accuracy. Significant challenges remain. For instance, our study's low rate of samples passing quality control highlights a marked difference in sample management between veterinary and human cancer care. Therefore, the pan-species digital pathology atlas, protocols and guidelines for veterinary pathologists provided in this study represent a big step towards rational and efficient transfer of AI technologies to veterinary medicine.

Another potential impact of this study is to empower precision medicine for treating animal cancers. Accurate diagnosis and timely treatment could be critical in preserving endangered and threatened species that represent important breeding populations[41]. We demonstrated how the AI tool can be used to study lymphocytic infiltration in canine transmissible venereal tumours and Tasmanian devil facial tumours with high accuracy and spatial resolution (Fig. 1B-C). As a transmissible disease, the immune response at the organismal level may offer new alternatives to understand the spread of the disease at a population scale from an epidemiological perspective[42,43]. These tumours can colonise a new host by crossing the barriers of histocompatibility associated with the immune system and expressing immunosuppressive cytokines[44,45]. The quantification and spatial detection of both tumour and immune cells can help study immune evasion and treatment in transmissible cancers, building on progress on understanding T cells immune infiltration in Tasmanian devils[46] and immune regulation in dog's CTVT tumour regression[47]. Furthermore, a detailed study of the tumour microenvironment can guide new discoveries to understand the mechanisms behind sensitivity and resistance to standard treatments such as chemotherapy,[4849]. By enabling precision medicine we can advance towards a more personalised and integrative approach to veterinary care[50].

Comparative oncology also brings tremendous benefits to human cancer research[5,51,52]. Our knowledge of cancer in wild animals is limited, and computational pathology can greatly expand research opportunities that compare cancer in the wild to managed populations, as well as comparisons with human cancer. Cross-species cancer comparisons may help address fundamental questions in cancer biology and evolution. This work revealed highly conserved morphology features across many species, particularly in epithelial and round-cell tumours, highlighting potential evolvability constraints for certain tumour types. The mismatch between species' evolutionary history and the conserved cellular morphological diversity raises new questions on the origin of cell morphological patterns; is morphological conservation fixed early in metazoan evolutionary history? Or is it the result of stabilising selection imposed by the extracellular matrix to meet homeostatic conditions?[53,54] Addressing the conserved features and differences in tumour biology can lead to novel research, therapeutics and discoveries that one day could be translated into human and non-human clinical care[37,55].

Limitations of this study include the limited availability of samples and annotations. It will be important to validate our findings on extended pan-species cohorts and advance our understanding of intratumor heterogeneity across different species and derive more controlled interspecies comparisons. With detailed multiplexing profiles, future attempts can shed more light on immune compositions in the microenvironment.

This work represents a step forward in incorporating machine learning in diagnostic investigations of natural and emerging diseases in animals, enhancing accuracy and sensitivity and complementing veterinary pathologists' capability in the decision-making process. Computational pathology can bring valuable opportunities for automated diagnosis, tumour grading, scoring, and precision medicine for animal cancers.

Materials and Methods

In total, 99 H&E samples from 29 species were identified from the Zoological Society of London's (ZSL) pathological archive, derived from clinical or postmortem examinations of ZSL London Zoo's living collections (Table S1). Of these, 51 slides from 22 species passed quality control for image analysis, and 18 slides representing 18 species were selected by the pathologists for subsequent analyses. Exclusion criteria were the lack of tumour components and the presence of high amounts of melanin/pigments in the tissue samples hindering the correct identification of individual cells. Samples were either obtained through tissue biopsies from surgery or routine postmortem examinations from animals that were i) examined directly after euthanasia or ii) stored at 4 degrees Celsius and examined within two days of death. A suspect tumour was removed, fixed in 10% buffered formalin solution and trimmed before being sent to external institutions (IZVG Pathology and Finn Pathologists) for histopathological processing, where they were subsequently embedded in paraffin blocks, sectioned and stained with H&E for analysis. Additionally, two samples were provided by the Transmissible Cancer Group, University of Cambridge, as previously reported in the following studies: *Canis familiaris* [56] and *Sarcophilus harrisii* [9].

All slides were scanned using NanoZoomer S210 digital slide scanner (C13239-01) and NanoZoomer digital pathology system v.3.1.7 (Hamamatsu) at 40X (228 nm/pixel resolution). The entire deep learning-based single-cell analysis pipeline described in [33] was implemented. This pipeline was designed and developed for human lung tumour specimens. Briefly, all 20 whole-section images were first down-scaled to ×20 and then tiled into 2000×2000 images for subsequent three-stage analysis. Firstly, all viable H&E tissue areas are segmented. Secondly, within the segmented tissue image, a spatially-constrained convolutional neural network predicts for each pixel the probability that it belongs to the centre of a nucleus; cell nuclei were then detected from the probability map obtained from the deep network. Lastly, each identified cell was classified using a neighbouring ensemble predictor coupled with a spatially constrained convolutional neural network. There were four cell classes: cancer (malignant epithelial) cells, lymphocytes (including plasma cells), noninflammatory stromal cells (fibroblasts and endothelial cells) and an 'other' cell type that included non-identifiable cells, less abundant cells such as macrophages and chondrocytes and 'normal' pneumocytes and bronchial epithelial cells.

Because the evaluation of the 'other' cell type class would be less mean, given the context of this study, we focused on the three main classes. Two board-certified specialist veterinary pathologists (CP and KH) annotated 14,570 cancer, lymphocyte and stromal single-cell annotations on raw whole-section images.

Features extraction at the cell level was done with two steps: a pre-trained MicroNet model[57] on lung H&Es to segment all cells, followed by automatic extraction of morphological measurements for the set of properties from each cell's mask. This allowed the extraction of 27 features for immune and tumour cells annotated by pathologists in the human and non-human slides (MATLAB function 'regionprops' with additional modifications as defined in Table S2). Annotated cells were mapped to the segmented cell centroid with a strict threshold of 4 pixels (< 2µm, which is less than 1/3 of a lymphocyte cell), and were visually assessed to confirm correct mapping. Dimension reduction was performed using principal component analysis. Then, we selected the first three dimensions of the PCA, enabling us to build a morphological volume for each cell class. We computed morphological space overlap using the R package 'dynRB', which calculates overlap based on the product of overlap at each dimension, the mean overlap across dimensions, or the geometrical mean across the PCA dimensions. We focus on quantifying the percentage of animal cells' morphological space that is covered by human cells' morphological space.

The algorithms' performance for detecting and classifying cells across all species was evaluated directly against the ground truth provided by pathologists' annotations. Individual class accuracy statistics were calculated using the R function 'confusionMatrix' from the R package 'caret'. To analyse the variability in the classification balanced accuracy values, BCAcc, across tumour or cell types, we fit a generalised linear model considering a beta distribution (logit link function) for continuous values between 0 and 1 (R package betareg). We computed likelihood ratio tests (R package lmtest) to evaluate if the distribution of balances accuracy between tumour types comes from the same χ^2 distribution. When the χ^2 test was significant ($p < 0.05$), we applied multiple comparisons correcting p-values using Tukey's procedures (R package emmeans). All the statistical tests were performed in R (version 4.0.3) and corresponding R codes are available at https://github.com/simonpcastillo/PanSpeciesHistology.

Tables

Table 1 Summary of overall balanced classification accuracy (BCAcc) by species. Balanced accuracy is computed as the average of sensitivity and specificity, 'overall' refers to the average of cancer, stromal and lymphocyte cells.

Code	Common name	Species	Diagnosis	Neoplasia site	Tumour type	Annotations	BCAcc
BITARI	Puff adder	*Bitis arietans*	Carcinoma	Pancreas	Epithelial	336	0.88
CANFAM	Dog	*Canis familiaris*	Canine transmissible venereal tumor	Intra vaginal	Round-cell	629	0.94
CAPHIR	West African pygmy goat	*Capra hircus*	Lymphosarcoma	Forestomach	Round-cell	965	0.70
CRAHEA	Panay cloudrunner	*Crateromys heaneyi*	Hepatocellular carcinoma	Liver	Epithelial	730	0.89
CYACYA	Red-legged honeycreeper	*Cyanerpes cyaneus*	Sertoli cell tumor	Testis	Sex-cord stromal	762	0.86
DASBYR	Kowari	*Dasyuroides byrnie*	Squamous cell carcinoma	Mouth	Epithelial	462	0.74
GALMOH	Greater bushbaby	*Galago moholi*	Squamous cell carcinoma	Skin	Epithelial	684	0.79
GONOXY	Redtailed ratsnake	*Gonyosoma oxycephala*	Metastatic anaplastic sarcoma	Multiple	Mesenchymal	526	0.91
LEMCAT	Ring-tailed lemur	*Lemur catta*	Haemangiosarcoma	Kidney	Mesenchymal	1049	0.79
LEOCHR	Golden-headed Lion Tamarin	*Leontopithecus chrysomelas*	Adenoma	Pituitary	Epithelial	601	0.94
LEPFAL	Mountain chicken frog	*Leptodactylus fallax*	Adenocarcinoma	Celomic cavity	Epithelial	740	0.81
MELURS	Sri Lankan sloth bear	*Melursus ursinus inornatus*	Pheochromocytoma	Adrenal	Neuroendocrine	959	0.88
MUSPUT	Domestic polecat	*Mustela putorius furo*	Sebaceous epithelioma	Skin	Epithelial	702	0.88

NASNAS	Brown-nosed coati	*Nasua nasua*	Lymphosarcoma	Multiple	Round-cell	520	0.57
OSTTET	West African dwarf crocodile	*Osteolaemus tetraspis tetraspis*	Lipoma	Liver	Neuroendocrine	1142	0.77
PANTRO	Chimpanzee	*Pan troglodytes*	Spindle cell tumor	Palate	Mesenchymal	866	0.75
SARHAR	Tasmanian devil	*Sarcophilus harrisii*	Devil facial tumor 1 (DFT1)	Hard palate near left side	Round-cell	484	0.88
SPHHUM	Humbolt penguin	*Spheniscus humboldti*	Renal cell adenoma	Kidney	Epithelial	452	0.72
SUSBAR	Bearded Pig	*Sus barbatus*	Adenocarcinoma	Uterus	Epithelial	1595	0.80
VARPRA	Emerald monitor	*Varanus prasinus*	Spindle cell sarcoma	Multiple	Mesenchymal	366	0.80

Figures

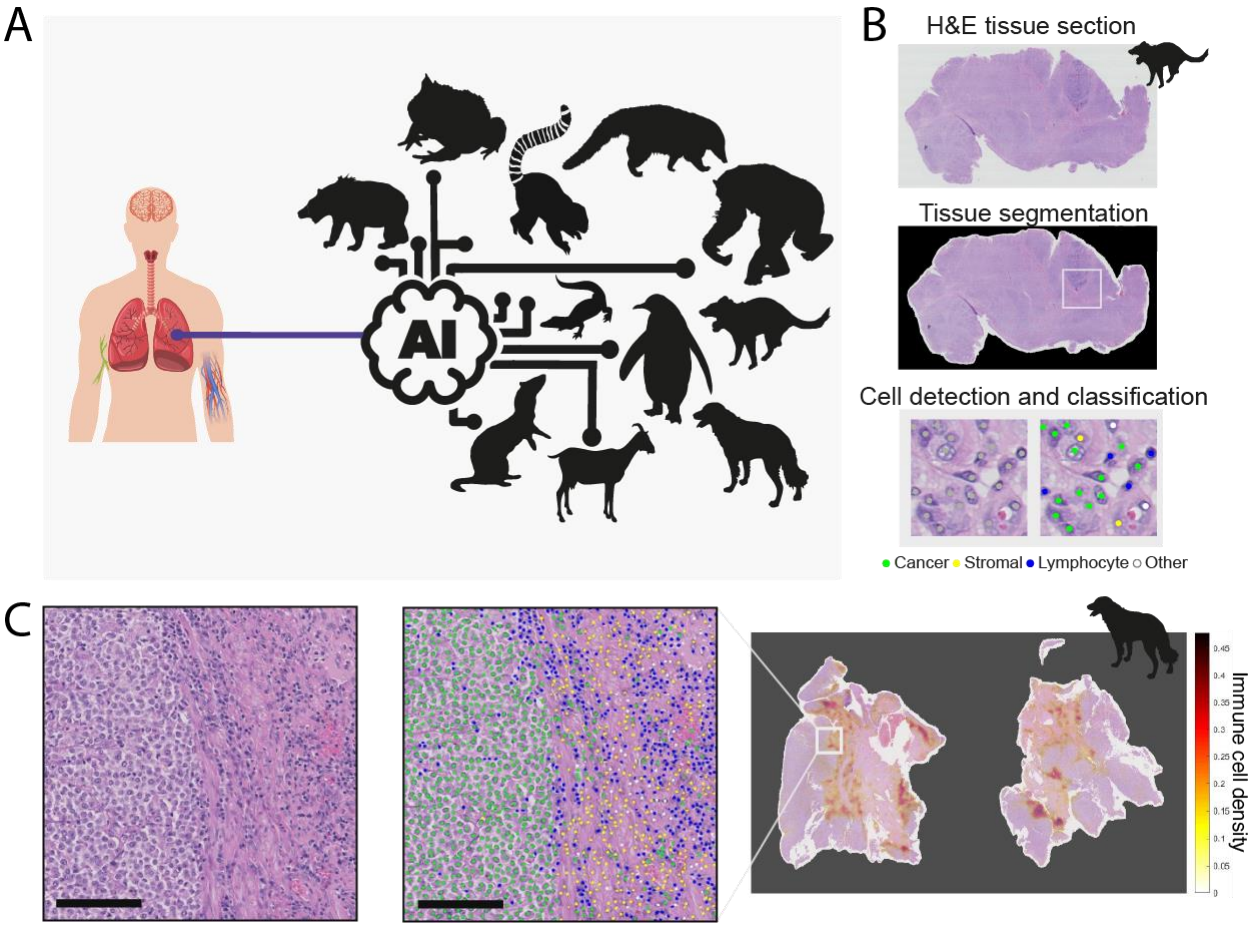

Figure 1 Pan-species computational pathology. (A) *Transfer learning* of cell identification from human lung to pan-species tumour pathology. (B) Overview of the H&E single-cell analysis pipeline illustrated from a Tasmanian devil's (SARHAR) facial tumour. This AI pipeline [33] first segments the viable tissue area, then detects and classifies all cells into cancer, stromal, lymphocyte and others. For more details, see Methods. (C) The same pipeline is implemented to spatially profile the immune microenvironment in a dog's (CANFAM) transmissible venereal tumour. Scale bar, 250 µm. Cell colours are denoted as four training classes, green: cancer (malignant epithelial) cells; blue: lymphocytes (including plasma cells); yellow: noninflammatory stromal cells (fibroblasts and endothelial cells); white: 'other' cell class that included nonidentifiable cells, less abundant cells such as macrophages and chondrocytes and 'normal' pneumocytes.

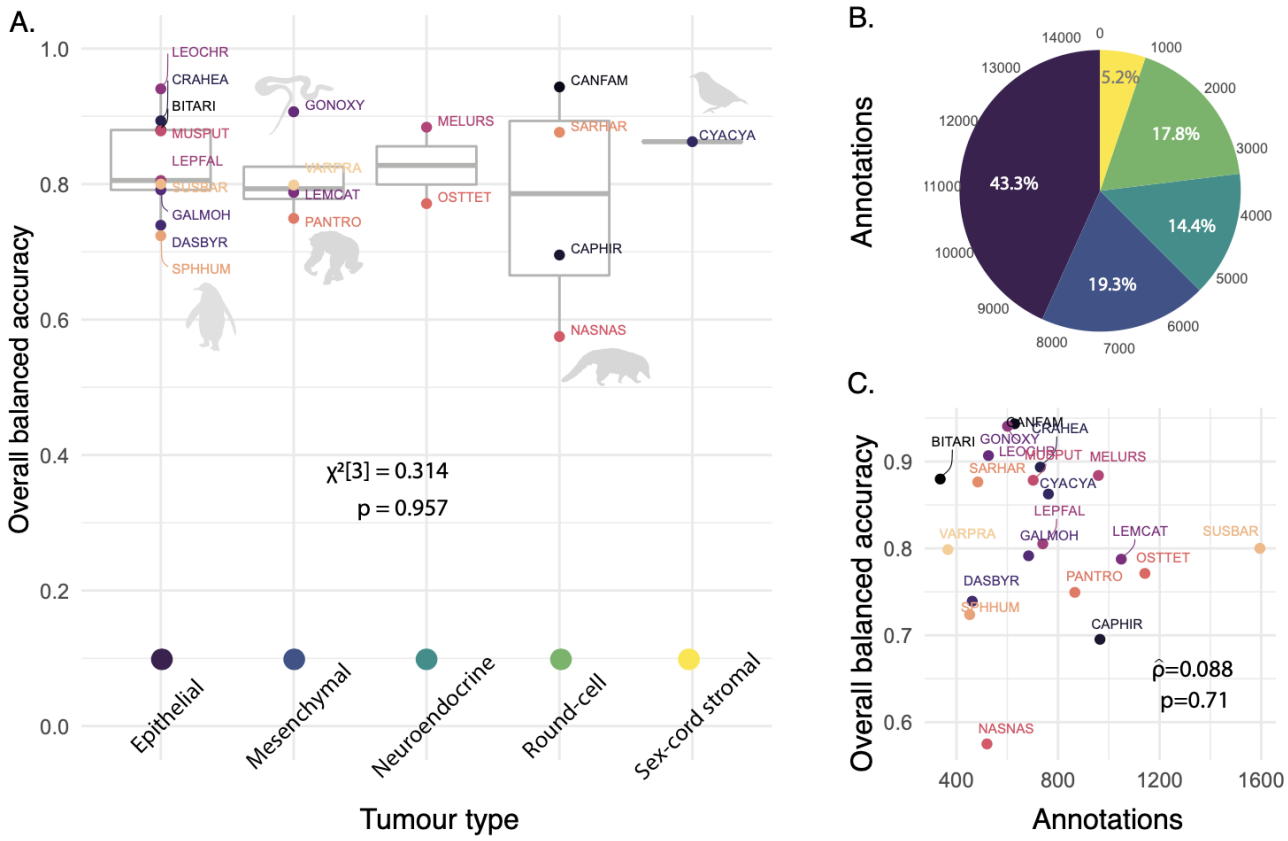

Figure 2 AI single-cell prediction comparison across tumour types. Balanced accuracy is computed as the average of sensitivity and specificity, 'overall' refers to the average of cancer, stromal and lymphocyte cells. (A) Pan-species overall balanced accuracy grouped by tumour type. (B) Distribution of the number of annotations by tumour type (colours correspond to tumour type in A). (C) Relationship between the number of annotations and the overall balanced accuracy for each species using Spearman's correlation. Species in (A) and (C) are labelled with their codes, for more species information, see Table 1.

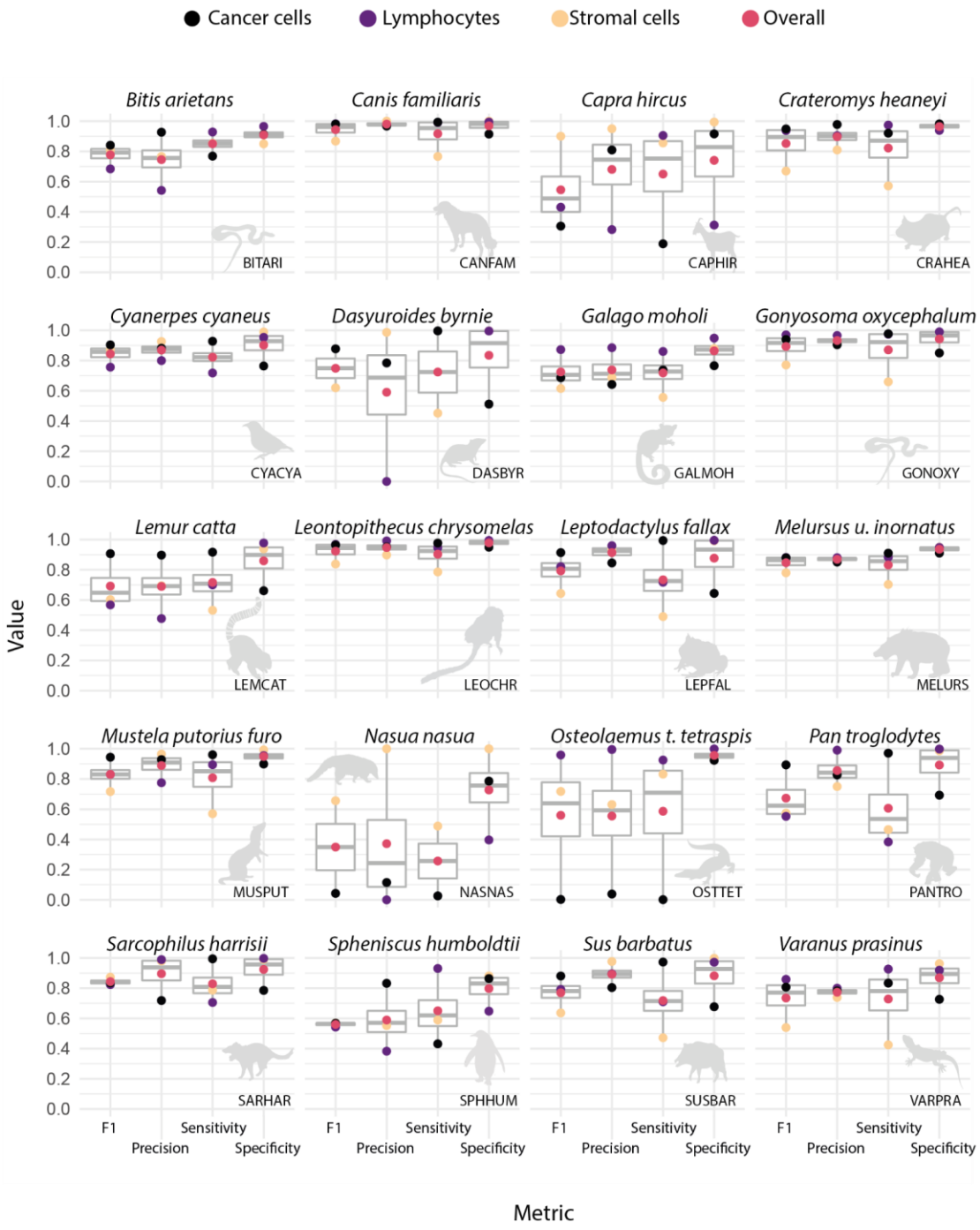

Figure 3 AI prediction variability for inter and intra- species tumour microenvironment cells. For each species, four metrics were evaluated including F1, precision, sensitivity and specificity (as labelled on the bottom x-axis) for the prediction accuracy of cancer, lymphocyte and stromal cells as well as their average shown as 'overall' (as denoted with colours on the top x-axis). For species codes, see Table 1.

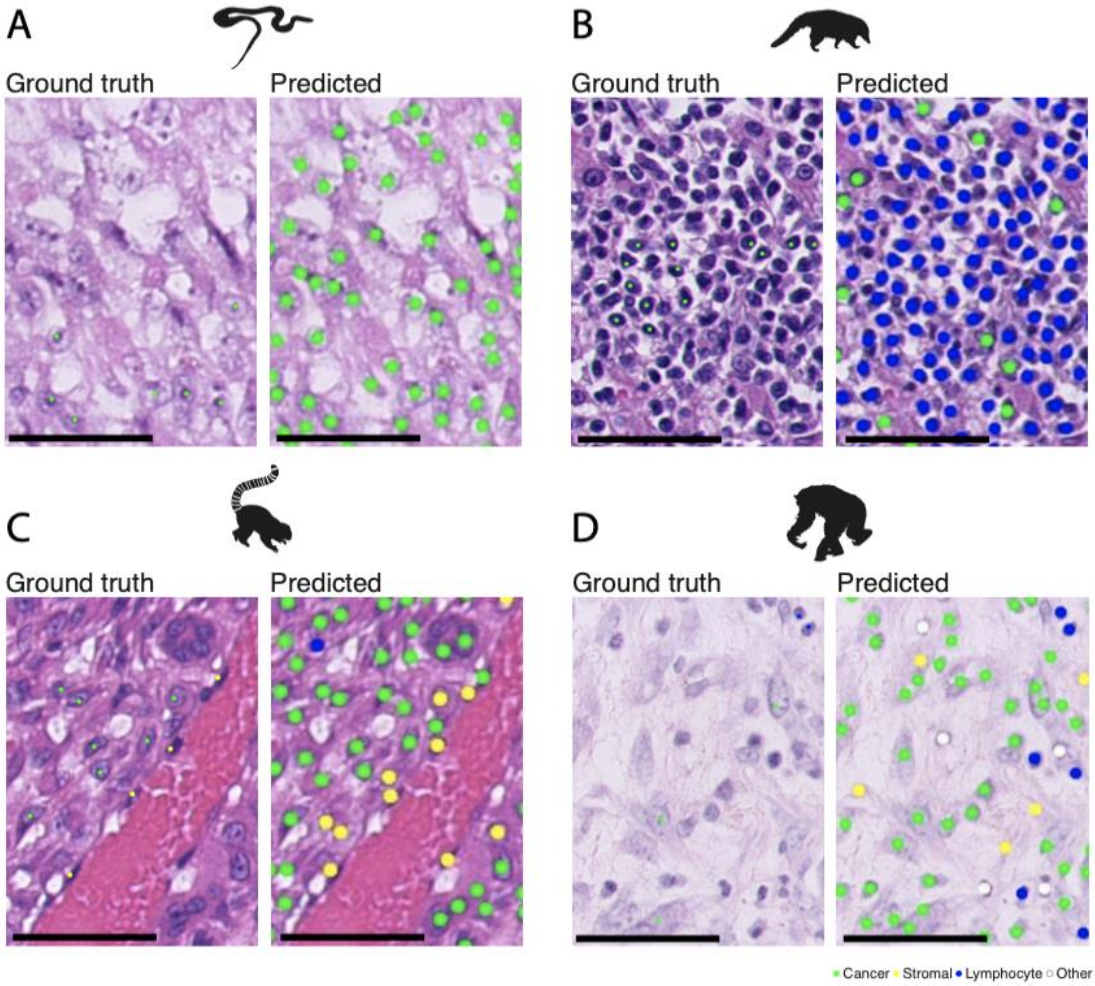

Figure 4 Strengths and pitfalls of current methods. Each H&E example is shown as a raw image with expert pathology annotations on some cells (left) and AI cell identification (right). Scale bar, 100 µm. Cell colours are denoted as four training classes, green: cancer (malignant epithelial) cells; blue: lymphocytes (including plasma cells); yellow: noninflammatory stromal cells (fibroblasts and endothelial cells); white: 'other' cell class that included nonidentifiable cells, less abundant cells such as macrophages and chondrocytes and 'normal' pneumocytes. (A) Correct identification of cancer cells from a mesenchymal tumour (metastatic anaplastic sarcoma) in a snake (GONOXY). (B) A challenging brown-nosed coati (NASNAS) case was diagnosed with a round-cell tumour (lymphosarcoma) where the cancer cell morphology is difficult to be recognised by an algorithm trained with epithelial cells from human lung cancer. (C) A malignant spindle cell tumour from a ring-tailed lemur (LEMCAT) with a haemangiosarcoma disease, as shown, the neoplastic endothelial cells have large rounded nuclei, which may appear morphologically similar to epithelial cancer cells, as opposed to the AI model's own normal -stromal- endothelial cells. However, the model successfully distinguished the majority of neoplastic from stromal cells. Further complexity is in the occurrence of epithelioid haemangiosarcoma where the cells of origin are endothelial cells but they actually become epithelial-like. (D) In the case of a chimpanzee (PANTRO) with a spindle cell sarcoma, the neoplastic fibroblasts are harder to differentiate from reactive fibroblasts.

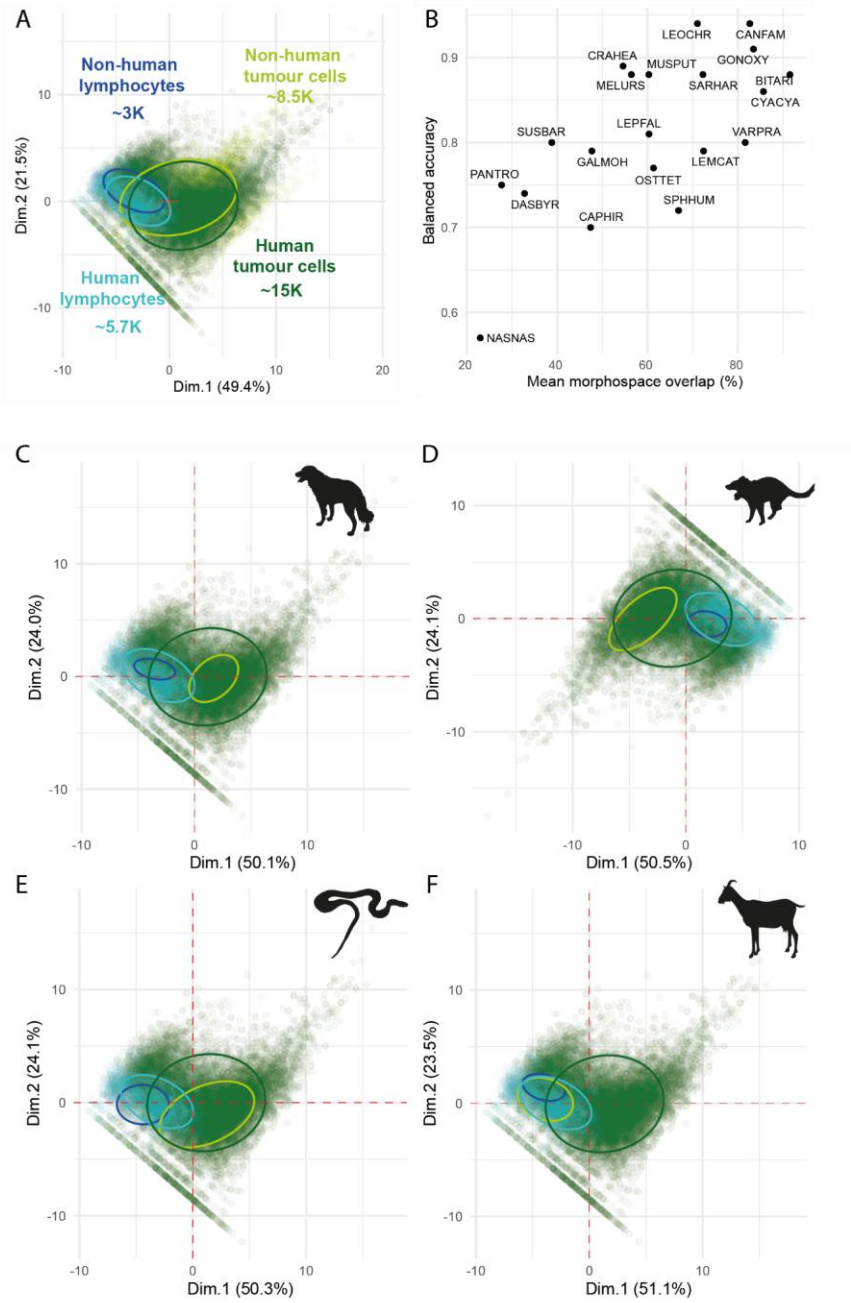

Figure 5 Overlap across the morphological space. (A) Overall high overlap between human and non-human cell morphologies across two dimensions of the principal component analysis, and their explained variances, of the morphological space made by ~31K cells annotated by pathologists. (B) the mean morphospace overlap across animal tumour cells and lymphocytes correlates with the model's balanced accuracy. (C-F) Species-specific morphological space overlap with human morphospace; (C) *Canis l. familiaris* (CANFAM), (D) *Sarcophilus harrisii* (SARHAR), (E) *Gonyosoma oxycephala* (GONOXY) and (F) *Capra hircus* (CAPHIR). Ellipses denote 95% of the distribution.

References

1. Aktipis, C. A. *et al.* Cancer across the tree of life: cooperation and cheating in multicellularity. *Phil. Trans. R. Soc. B* **370**, 20140219 (2015).
2. Kitsoulis, C. V., Baxevanis, A. D. & Abatzopoulos, T. J. The occurrence of cancer in vertebrates: a mini review. *J of Biol Res-Thessaloniki* **27**, 9 (2020).
3. Aktipis, C. A. & Nesse, R. M. Evolutionary foundations for cancer biology. *Evol Appl* **6**, 144–159 (2013).
4. Hughes, K. Comparative mammary gland postnatal development and tumourigenesis in the sheep, cow, cat and rabbit: Exploring the menagerie. *Seminars in Cell & Developmental Biology* **114**, 186–195 (2021).
5. Abegglen, L. M. *et al.* Potential Mechanisms for Cancer Resistance in Elephants and Comparative Cellular Response to DNA Damage in Humans. *JAMA* **314**, 1850–1860 (2015).
6. Sulak, M. *et al.* TP53 copy number expansion is associated with the evolution of increased body size and an enhanced DNA damage response in elephants. *eLife* **5**, e11994 (2016).
7. Shao, Y. W. *et al.* Cross-species genomics identifies DLG2 as a tumor suppressor in osteosarcoma. *Oncogene* **38**, 291–298 (2019).
8. Wong, K. *et al.* Cross-species genomic landscape comparison of human mucosal melanoma with canine oral and equine melanoma. *Nature Communications* **10**, 353 (2019).
9. Stammnitz, M. R. *et al.* The Origins and Vulnerabilities of Two Transmissible Cancers in Tasmanian Devils. *Cancer Cell* **33**, 607-619.e15 (2018).
10. Murchison, E. P. Clonally transmissible cancers in dogs and Tasmanian devils. *Oncogene* **27**, S19–S30 (2008).
11. Dujon, A. M. *et al.* Transmissible Cancers in an Evolutionary Perspective. *iScience* **23**, 101269 (2020).
12. Pi Castro, D. *et al.* Expression of FOXP3 in Canine Gliomas: Immunohistochemical Study of Tumor-Infiltrating Regulatory Lymphocytes. *Journal of Neuropathology & Experimental Neurology* **79**, 184–193 (2020).
13. Aubreville, M. *et al.* A completely annotated whole slide image dataset of canine breast cancer to aid human breast cancer research. *Scientific Data* **7**, 417 (2020).
14. Gardner, H. L., Fenger, J. M. & London, C. A. Dogs as a Model for Cancer. *Annual Review of Animal Biosciences* **4**, 199–222 (2016).
15. Pesavento, P. A., Agnew, D., Keel, M. K. & Woolard, K. D. Cancer in wildlife: patterns of emergence. *Nat Rev Cancer* **18**, 646–661 (2018).
16. Browning, H. M., Gulland, F. M. D., Hammond, J. A., Colegrove, K. M. & Hall, A. J. Common cancer in a wild animal: the California sea lion (Zalophus californianus) as an emerging model for carcinogenesis. *Philos Trans R Soc Lond B Biol Sci* **370**, (2015).

17. Chang, P. H. *et al.* Spontaneous neoplasms in zoo mammals, birds, and reptiles in Taiwan - A 10-year survey. *Animal Biology* **62**, 95–110 (2012).
18. Madsen, T. *et al.* Cancer Prevalence and Etiology in Wild and Captive Animals. *Ecology and Evolution of Cancer* 11–46 (2017) doi:10.1016/B978-0-12-804310-3.00002-8.
19. Boddy, A. M. *et al.* Lifetime cancer prevalence and life history traits in mammals. *Evolution, Medicine, and Public Health* **2020**, 187–195 (2020).
20. Junginger, J. *et al.* Pathology in Captive Wild Felids at German Zoological Gardens. *PLOS ONE* **10**, e0130573 (2015).
21. McAloose, D. & Newton, A. L. Wildlife cancer: a conservation perspective. *Nat Rev Cancer* **9**, 517–526 (2009).
22. Tuia, D. *et al.* Perspectives in machine learning for wildlife conservation. *Nat Commun* **13**, 792 (2022).
23. Boddy, A. M., Harrison, T. M. & Abegglen, L. M. Comparative Oncology: New Insights into an Ancient Disease. *iScience* **23**, 101373 (2020).
24. Bertram, C. A. & Klopfleisch, R. The Pathologist 2.0: An Update on Digital Pathology in Veterinary Medicine. *Vet Pathol* **54**, 756–766 (2017).
25. Zuraw, A. & Aeffner, F. Whole-slide imaging, tissue image analysis, and artificial intelligence in veterinary pathology: An updated introduction and review. *Vet Pathol* **59**, 6–25 (2022).
26. Hoenerhoff, M. J., Meyerholz, D. K., Brayton, C. & Beck, A. P. Challenges and Opportunities for the Veterinary Pathologist in Biomedical Research. *Vet Pathol* **58**, 258–265 (2021).
27. Meuten, D. J. *et al.* International Guidelines for Veterinary Tumor Pathology: A Call to Action. *Vet Pathol* **58**, 766–794 (2021).
28. Ezanno, P. *et al.* Research perspectives on animal health in the era of artificial intelligence. *Vet Res* **52**, 40 (2021).
29. Aubreville, M. *et al.* Deep learning algorithms out-perform veterinary pathologists in detecting the mitotically most active tumor region. *Scientific Reports* **10**, 16447 (2020).
30. Nagy, D. *et al.* Developing ovine mammary terminal duct lobular units have a dynamic mucosal and stromal immune microenvironment. *Commun Biol* **4**, 993 (2021).
31. Awaysheh, A. *et al.* Evaluation of supervised machine-learning algorithms to distinguish between inflammatory bowel disease and alimentary lymphoma in cats. *J VET Diagn Invest* **28**, 679–687 (2016).
32. Mattoon, J. S. & Bryan, J. N. The future of imaging in veterinary oncology: Learning from human medicine. *The Veterinary Journal* **197**, 541–552 (2013).
33. AbdulJabbar, K. *et al.* Geospatial immune variability illuminates differential evolution of lung adenocarcinoma. *Nature Medicine* **26**, 1054–1062 (2020).

34. Elyada, E. *et al.* Cross-Species Single-Cell Analysis of Pancreatic Ductal Adenocarcinoma Reveals Antigen-Presenting Cancer-Associated Fibroblasts. *Cancer Discov* **9**, 1102–1123 (2019).
35. Montali, R. J. Comparative pathology of inflammation in the higher vertebrates (reptiles, birds and mammals). *Journal of Comparative Pathology* **99**, 1–26 (1988).
36. Syrykh, C. *et al.* Accurate diagnosis of lymphoma on whole-slide histopathology images using deep learning. *npj Digital Medicine* **3**, 1–8 (2020).
37. Mestrinho, L. A. & Santos, R. R. Translational oncotargets for immunotherapy: From pet dogs to humans. *Advanced Drug Delivery Reviews* **172**, 296–313 (2021).
38. Dobson, J. M. Significant advances in veterinary oncology – 60 years on. *Journal of Small Animal Practice* **60**, 711–722 (2019).
39. Gyles, C. Meeting demands in specialist training — whose responsibility? *Can Vet J* **50**, 687–690 (2009).
40. Riccardo, F., Aurisicchio, L., Impellizeri, J. A. & Cavallo, F. The importance of comparative oncology in translational medicine. *Cancer Immunol Immunother* **64**, 137–148 (2015).
41. McCallum, H. Tasmanian devil facial tumour disease: lessons for conservation biology. *Trends in Ecology & Evolution* **23**, 631–637 (2008).
42. Ujvari, B., Gatenby, R. A. & Thomas, F. The evolutionary ecology of transmissible cancers. *Infection, Genetics and Evolution* **39**, 293–303 (2016).
43. Jones, E. A., Cheng, Y. & Belov, K. The origin, dynamics, and molecular evolution of transmissible cancers. *AGG* **5**, 317–326 (2015).
44. Patchett, A. & Woods, G. Targeting transmissible cancers in animals. *Science* **365**, 438–440 (2019).
45. Siddle, H. V. & Kaufman, J. Immunology of naturally transmissible tumours. *Immunology* **144**, 11–20 (2015).
46. Pye, R. *et al.* Demonstration of immune responses against devil facial tumour disease in wild Tasmanian devils. *Biology Letters* **12**, 20160553 (2016).
47. Frampton, D. *et al.* Molecular Signatures of Regression of the Canine Transmissible Venereal Tumor. *Cancer Cell* **33**, 620-633.e6 (2018).
48. Hui, L. & Chen, Y. Tumor microenvironment: Sanctuary of the devil. *Cancer Letters* **368**, 7–13 (2015).
49. Klopfleisch, R., Kohn, B. & Gruber, A. D. Mechanisms of tumour resistance against chemotherapeutic agents in veterinary oncology. *The Veterinary Journal* **207**, 63–72 (2016).
50. Klopfleisch, R. Personalised medicine in veterinary oncology: One to cure just one. *The Veterinary Journal* **205**, 128–135 (2015).
51. Nunney, L., Maley, C. C., Breen, M., Hochberg, M. E. & Schiffman, J. D. Peto's paradox and the promise of comparative oncology. *Philosophical Transactions of the Royal Society B: Biological Sciences* **370**, 20140177 (2015).

52. Schiffman, J. D. & Breen, M. Comparative oncology: what dogs and other species can teach us about humans with cancer. *Philosophical Transactions of the Royal Society B: Biological Sciences* **370**, 20140231 (2015).
53. Bissell, M. J. & Barcellos-Hoff, M. H. The Influence of Extracellular Matrix on Gene Expression: Is Structure the Message? *Journal of Cell Science* **1987**, 327–343 (1987).
54. Watt, F. M. The extracellular matrix and cell shape. *Trends in Biochemical Sciences* **11**, 482–485 (1986).
55. Klingemann, H. Immunotherapy for Dogs: Running Behind Humans. *Front Immunol* **9**, 133 (2018).
56. Strakova, A. *et al.* Recurrent horizontal transfer identifies mitochondrial positive selection in a transmissible cancer. *Nat Commun* **11**, 3059 (2020).
57. Raza, S. E. A. *et al.* Micro-Net: A unified model for segmentation of various objects in microscopy images. *Medical Image Analysis* **52**, 160–173 (2019).

Acknowledgements:

The authors wish to thank Edmund Flach from the Zoological Society of London, as well as external pathologists Mark Stidworthy, Daniella Denk, Cheryl Sangster, and Ann Pocknell. LMA acknowledges support from the Department of Pediatrics Research Enterprise (University of Utah). Figure icons were taken from phylopic.org (CC BY 3.0), thanks to Sarah Werning, Rebecca Groom, T. Michael Keesey and Tony Hisgett.

Funding:

The Arizona Cancer Evolution Center, University of Arizona, USA.

National Institutes of Health grant U54 CA217376 (YY, AMB, LMA, TAG)

National Institutes of Health grant R01 CA185138 (YY)

Cancer Research UK Career Establishment Award C45982/A21808 (YY)

Cancer Research UK Early Detection Program Award C9203/A28770 (YY)

Cancer Research UK Sarcoma Accelerator C56167/A29363 (YY)

Cancer Research UK Brain tumour Award C25858/A28592 (YY, SPC)

Rosetrees Trust A2714 (YY)

Children's Cancer and Leukaemia Group CCLGA201906 (YY)

The Royal Marsden Hospital, the ICR National Institute of Health Research Biomedical Research Centre (YY).

Department of Pediatrics Research Enterprise, University of Utah (LMA)

Author contributions:

Conceptualization: KA, SPC, EPM, TAG, CP, YY; Methodology: KA, SPC, CP, KH, HD, SS, EF; Investigation: KA, SPC, CP, YY; Writing: SPC, KA, YY, AMB, LMA, CP, YY, with input from all authors.

Competing interests:

The funders had no role in the design of the study; the collection, analysis, or interpretation of the data; the writing of the manuscript; or the decision to submit the manuscript for publication.

Y.Y. has received speakers bureau honoraria from Roche and consulted for Merck and Co Inc. L.M.A. is a share-holder and consultant to PEEL Therapeutics, Inc.

Data and materials availability:

The deep-learning pipeline for digital pathology image analysis is previously available for non-commercial research purposes at https://github.com/qalid7/compath. All code used for statistical analyses of image data and morphospace overlap test tool was developed in R (v.4.0.3) and it is available at https://github.com/simonpcastillo/PanSpeciesHistology. A rich, pan-species digital pathology atlas will be made publicly available upon publication, providing pan-species digital slide images, slide digitalisation and quality control protocols, and pathological annotations of 14,570 single-cell annotations across 20 species.

Supplementary

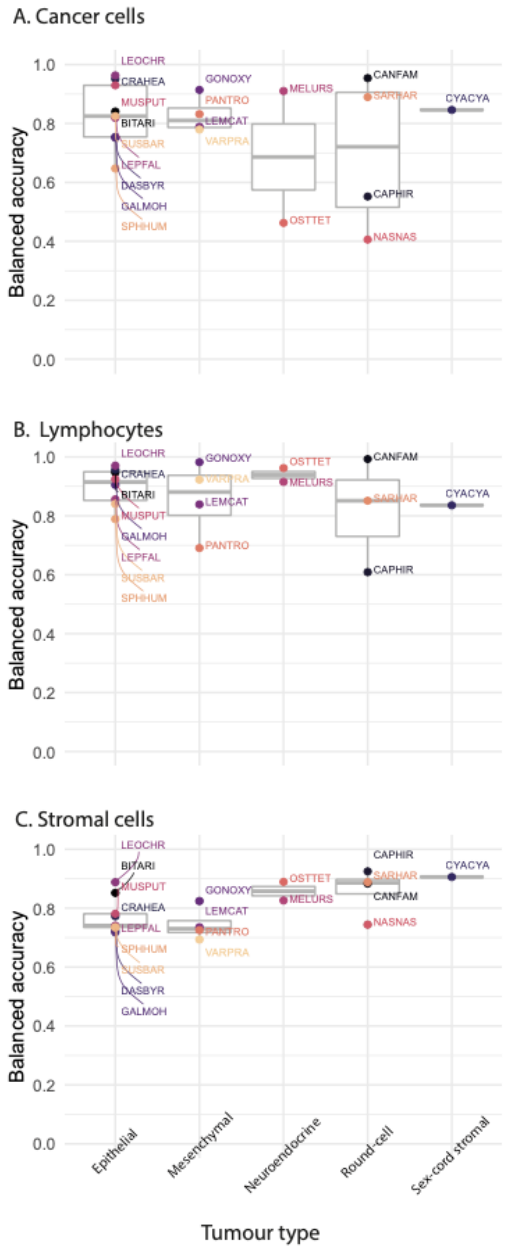

Supplementary Figure 1 Extended AI single-cell prediction comparison across tumour types. Balanced accuracy is computed as the average of sensitivity and specificity for (A) cancer, (B) stromal and (C) lymphocyte cells for all species. Species are grouped according to their tumour type and are labelled with their codes, for more species information, see Table 1.

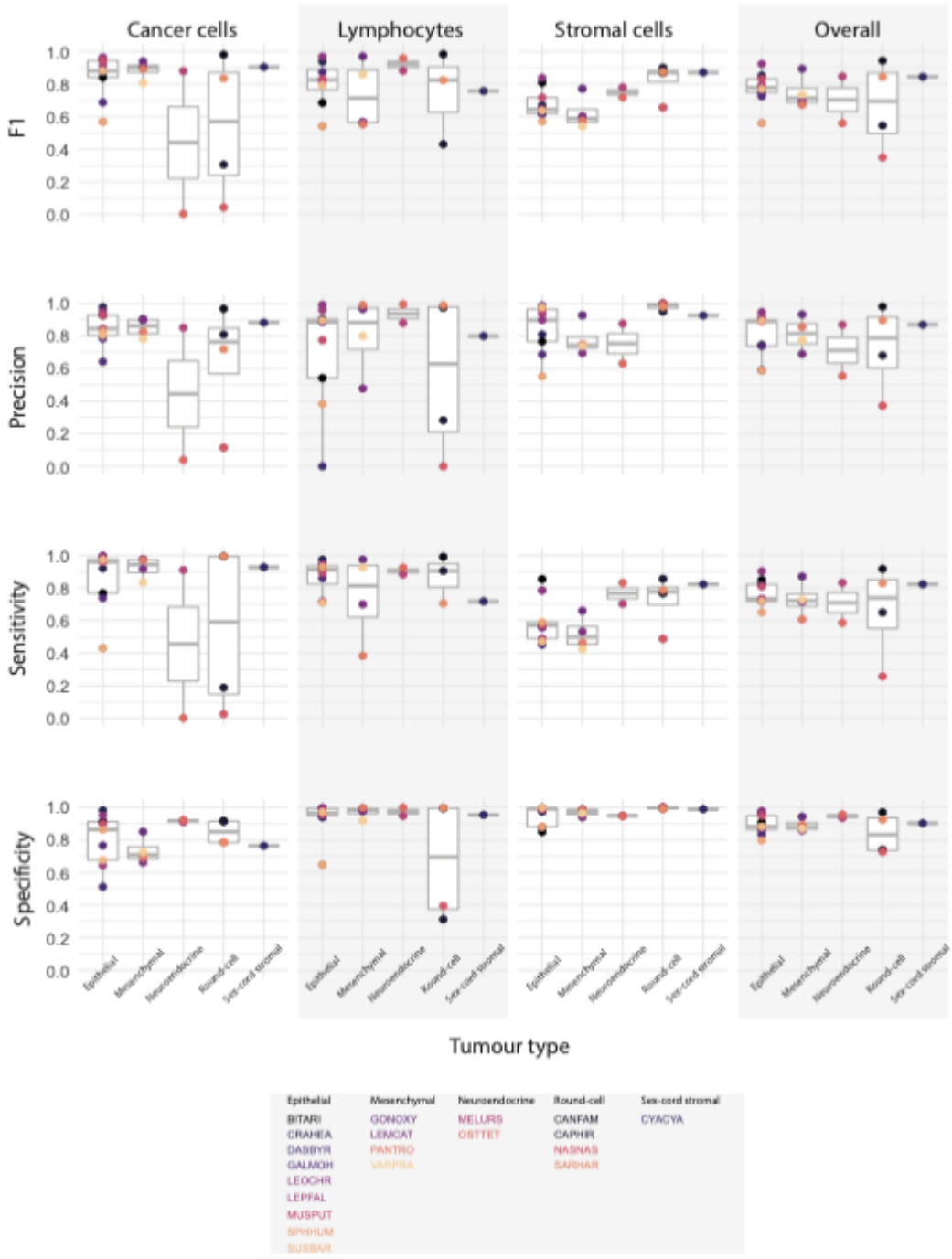

Supplementary Figure 2 Extended AI prediction variability for inter and intra- species tumour microenvironment cells. For each species, four metrics were evaluated including F1, precision, sensitivity and specificity (rows) for the prediction accuracy of cancer, lymphocyte and stromal cells as well as their average shown as 'overall' (columns). Species are grouped according to their tumour type and are labelled with their codes, for more species information, see Table 1.

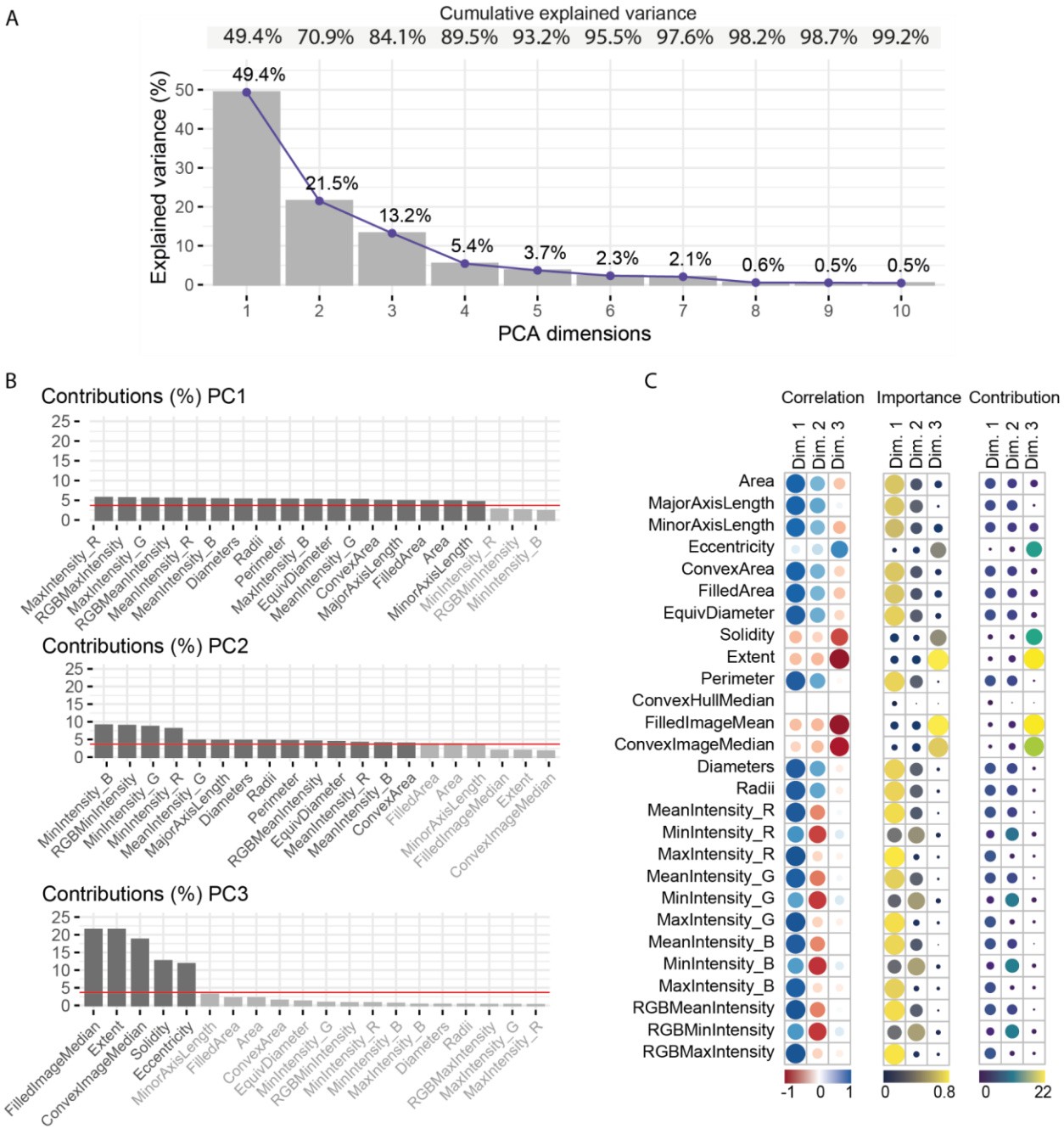

Supplementary Figure 3 Analysis of the morphological space. (A) Dimensions of the principal component analysis (PCA) and their explained variances. (B) The highest 20 contributions to PCA dimensions' explained variances. Darker bars are features above the mean contribution (red line). (C) From left to right, correlation, importance and contribution of the single-cell morphological features to PCA dimension.

Supplementary Table 1 Summary of sample preparation methods as provided from the Zoological Society of London's pathological archive.

Case ID	Species code	Pathologists	Method
B01/17	MUSPUT	IZVG/RVC- DD	Biopsy: removed during surgery and formalin-fixed
B02/18	GALMOH	IZVG/RVC- DD	Biopsy: removed during surgery and formalin-fixed
B04/17	LEMCAT	IZVG/RVC- MS	Biopsy: removed during surgery and formalin-fixed
B07-8/04	PANTRO	ZSL- AP	Biopsy - removed during surgery and formalin-fixed
B09/04	DASBYR	ZSL- AP	Biopsy - removed during surgery and formalin-fixed
W17M035	MELURS	IZVG/RVC- MS	Euthanasia: Carcass fresh – PM examination one day after death
W17R187	OSTTET	IZVG/RVC- DD	Natural death: Carcass fresh - PM on day of death
ZA1360/15	LEPFAL	IZVG/RVC- MS	Natural death: Carcass slightly autolysed – PM on day of death
ZB017/18	CYACYA	IZVG/RVC- MS	Euthanasia: Carcass fresh – PM examination one day after death
ZB485/19	SPHHUM	IZVG/RVC- CS	Euthanasia: No comment on carcass condition - PM carried out 2 days after euthanasia
ZM134/17	CAPHIR	IZVG/RVC- CS	Carcass fresh – euthanised and PM'd on day of death
ZM138/17	SUSBAR	IZVG/RVC- MS	Carcass fresh - PM on day of death
ZM203/17	LEOCHR	IZVG/RVC- MS	Carcass fresh - PM on day of death
ZM633/18	CRAHEA	IZVG/RVC- DD	Euthanasia: Carcass fresh – PM examination one day after death
ZM748/18	NASNAS	IZVG/RVC- CS	Euthanasia: Carcass fresh – PM examination one day after death
ZR1145/15	GONOXY	IZVG/RVC- MS	Euthanasia: Carcass fresh - kept in fridge two days before examination

ZR1148/18	VARPRA	IZVG/RVC- DD	Euthanasia: Carcass fresh – PM examination one day after death
ZR474/19	BITARI	IZVG/RVC- CS	Euthanasia: Carcass fresh – PM examination one day after death

Supplementary Table 2 The 27 single-cell features extracted to compute the morphological space.

Feature	Description
Area	Two-dimensional extension of a shape
MajorAxisLength	Longest diameter
MinorAxisLength	Shortest diameter
Eccentricity	Magnitude inversely related to shape curvature
ConvexArea	Area resulting from connecting the external points of the shape
FilledArea	Area of a corresponding image with holes filled in
EquivDiameter	Diameter of a circle with the same area as the region
Solidity	Extent to which the shape fills the convex area
Extent	Ratio of pixels in the region to pixels in the total bounding box
Perimeter	Length of the shape boundary
ConvexHullMean	Smallest convex polygon that can contain the region
FilledImageMean	Average of pixels corresponding to the segmented mask, with all holes filled
ConvexImageMean	Average of pixels corresponding to a segmented mask which specifies the convex hull of the region
Diameters	Cell diameter using major and minor axes
Radii	Cell radius
MeanIntensity_R	Mean pixel intensity in the red channel
MinIntensity_R	Minimum pixel intensity in the red channel
MaxIntensity_R	Maximum pixel intensity in the red channel

MeanIntensity_G	Mean pixel intensity in the green channel
MinIntensity_G	Minimum pixel intensity in the green channel
MaxIntensity_G	Maximum pixel intensity in the green channel
MeanIntensity_B	Mean pixel intensity in the blue channel
MinIntensity_B	Minimum pixel intensity in the blue channel
MaxIntensity_B	Maximum pixel intensity in the blue channel
RGBMeanIntensity	Mean pixel intensity in the composed image
RGBMinIntensity	Minimum pixel intensity in the composed image
RGBMaxIntensity	Maximum pixel intensity in the composed image

Supplementary table 3 Morphological volumes overlap of human cells on non-human cells' morphological space calculated by the three methods. The highest overlap values for non-human lymphocytes and tumour cells are bold-faced.

Morphological volume of	Covered by the volume of	% Overlap (product)	% Overlap (mean)	% Overlap (geom. mean)
Non-human lymphocytes	**Human lymphocytes**	**63.47**	**84.55**	**81.25**
Non-human lymphocytes	Human tumour cells	40.41	67.6	59.84
Non-human tumour cells	Human lymphocytes	16.56	54.82	50.24
Non-human tumour cells	**Human tumour cells**	**67.97**	**86.49**	**86.14**